

Sensitivity analysis and automation for intraoperative implementation of the atlas-based method for brain shift correction

Ishita Chen^a, Amber L. Simpson^a, Kay Sun^a, Reid C. Thompson,^{a,c} and Michael I. Miga ^{*a,b,c}
^aDepartment of Biomedical Engineering, Vanderbilt University, Nashville, TN, ^bDepartment of Radiology and Radiological Sciences, Vanderbilt University Medical Center, Nashville, TN, ^cDepartment of Neurological Surgery, Vanderbilt University Medical Center, Nashville, TN

*Michael.I.Miga@vanderbilt.edu; Phone: 615-343-8336; Web: <http://bmlweb.vuse.vanderbilt.edu>

ABSTRACT

The use of biomechanical models to correct the misregistration due to deformation in image guided neurosurgical systems has been a growing area of investigation. In previous work, an atlas-based inverse model was developed to account for soft-tissue deformations during image-guided surgery. Central to that methodology is a considerable amount of pre-computation and planning. The goal of this work is to evaluate techniques that could potentially reduce that burden. Distinct from previous manual techniques, an automated segmentation technique is described for the cerebrum and dural septa. The shift correction results using this automated segmentation method were compared to those using the manual methods. In addition, the extent and distribution of the surgical parameters associated with the deformation atlas were investigated by a sensitivity analysis using simulation experiments and clinical data. The shift correction results did not change significantly using the automated method (correction of $73\pm 13\%$) as compared to the semi-automated method from previous work (correction of $76\pm 13\%$). The results of the sensitivity analysis show that the atlas could be constructed by coarser sampling (six fold reduction) without substantial degradation in the shift reconstruction, a decrease in preoperative computational time from 13.1 ± 3.5 hours to 2.2 ± 0.6 hours. The automated segmentation technique and the findings of the sensitivity study have significant impact on the reduction of pre-operative computational time, improving the utility of the atlas-based method. The work in this paper suggests that the atlas-based technique can become a 'time of surgery' setup procedure rather than a pre-operative computing strategy.

Keywords: Image guided surgery, neurosurgery, atlas-based model, biomechanical model, segmentation, sensitivity analysis

1. INTRODUCTION

It is now recognized that intraoperative neurosurgical guidance systems can be compromised by non-rigid brain deformations caused by gravitational forces, administration of hyperosmotic drugs like mannitol, swelling, resection and retraction forces [1, 2]. This is the brain shift problem. The misregistration between physical and image space that is associated with this problem usually ranges from 1 to 2.5 cm [1-3]. Various techniques to correct for this misregistration span from acquisition of volumetric intraoperative images like computed tomography (CT) [4], magnetic resonance imaging (MRI) [2], ultrasound [5-7], and predictive biomechanical modeling [8-12]. While several medical centers have adopted the direct usage of intraoperative imaging units for guidance, there is still a need to register the wealth of preoperative data that cannot be obtained during surgery (e.g. diffusion tensor MR or functional MR). Methods to achieve this during the procedure have been forthcoming and represent data-rich frameworks [8, 10, 13]. However, concerns like exposure to ionizing radiation for CT and prohibitively high expense for MRI have led others to pursue more cost efficient methods using sparse intraoperative imaging devices like stereoscopic operating microscopes [14], laser range scanner devices [15, 16], and ultrasound imaging [5-7]. These devices provide information at the exposed craniotomy surface, some subsurface information in the case of ultrasound, and are often coupled with computer models (either biomechanical or interpolative) to provide deformation information in the rest of the domain [3, 7, 12, 17].

The physical properties that govern the brain tissue deformation have been described using different constitutive laws – linear elastic [8, 10], non-linear viscoelastic [9], and biphasic [11]. While the complex non-linear model may describe

the physical interaction of tissue more accurately, the complexity may come at the cost of computational time, which may be a hindrance in its implementation in real time. In addition, from the systems level perspective, often the error between linear and nonlinear models is small compared to the errors associated with tracking and segmentation. Nevertheless, regardless of the choice of model, with sparse intraoperative data, there is considerable uncertainty in the determination of factors that cause deformation to exact precision in the OR. These factors can be the head orientation, level of cerebrospinal fluid (CSF) drainage, and the alteration of capillary permeability resulting from administration of mannitol. To circumvent these problems, Dumpuri et. al. proposed an atlas-based approach where the forward model for deformation was solved for different permutations of driving conditions [12]. Minimization of the least squared error between the model predictions and the sparse intraoperative measurements provided the final solution. In this particular work, the biphasic model based on Biot's consolidation theory [18] was used to describe the physical behavior of brain tissue. Discretized and solved with the Galerkin weighted residual method in finite element analysis, this model was ideally suited for the atlas based approach because of computational simplicity while taking into account the role of interstitial pressure driving fluid movement in brain tissue.

The atlas based method was validated with pre- and post-operative MR data. The atlas-based model provided an average of 85% surface and subsurface shift correction [17]. The method was also evaluated with intraoperative data in [3] and the shift correction was found to be an average of 75%. The reason for the degradation of correction in intraoperative data was the larger magnitude of shift correction and the more dynamic interactions like resection forces in the OR, as compared to the post-operative MR, where the time elapsed after the surgery allowed for shift recovery. There was also a suggestion in [3] that mannitol played a more considerable role in the magnitude of deformation whereas it would not have been as pronounced in the Dumpuri et al. study [17]. The work presented in [17] and [3] was a retrospective analysis and important issues of intraoperative implementation were not addressed in that work. For instance, both the works described segmenting the brain and building a patient specific mesh from the MRI scans acquired for every patient. In addition, the work in [3] suggested the need to model the dural septa, membranous structures like the falx cerebri and the tentorium cerebella, that limit the movement of brain in the contra-lateral hemisphere and the cerebellar region of the brain. The method of segmentation of the brain and the dural septa was a manual and tedious process. While the mesh creation and the atlas building computations are done pre-operatively, the time window between image acquisition and surgery can be a few hours. For the method to be feasible for clinical implementation, automating the processes to reduce computation time may be critical. This paper will look at an automatic segmentation method for the cerebral tissue and the dural septa and compare the results to the manual segmentation.

The atlas of deformations in [17] was formed with gravity, mannitol, and swelling driving conditions and consisted of 501 solutions. The results in that paper showed a very minor role of swelling in the reconstructed solutions, and the analysis in [3] only consisted of gravity and mannitol solutions, with and without tumor resection – a total of 720 solutions. While shift reconstruction in the OR using the atlas takes under a minute, the pre-operative time required to build the atlas on a parallel cluster ranges from 10 to 18 hours, depending on the number of solutions. The size of the atlases in the above two papers was not extensively analyzed. One aspect to this paper will be to investigate the level of detail used in the atlas-based method within the context of shift prediction and determine what resolution of atlas is necessary. Building atlases with fewer solutions could have a significant impact on the computation time to construct the atlas. In this paper, results of systematic sensitivity studies towards the automation of our segmentation approaches and the effects of atlas resolution will be investigated with respect to the prediction accuracy of our approach.

2. METHODS

A semi-automated pipeline that consists of manual image segmentation, semi-automated dural septa segmentation, mesh generation, atlas building using forward model runs of the linear elastic biphasic model, and inverse solution using optimized linear least squared error between atlas predictions and sparse measurements was presented in [3]. The first four steps are performed pre-operatively after the patient MRI images are acquired. The inverse model is solved intraoperatively after acquisition of sparse serial LRS scans before and after tumor resection. The schematic of the process is shown in Figure 1.

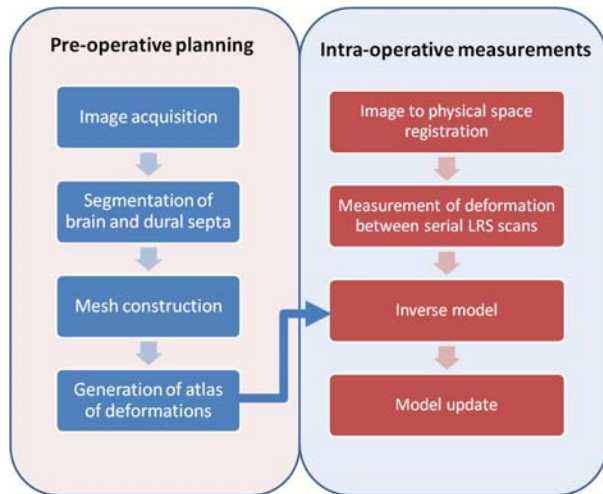


Figure 1: Schematic of the pipeline for model updated image guidance system. The pre-operative computations are typically performed the day before surgery and take on the order of several hours of computation. The intraoperative computations are performed during the surgery and provide updated information in real time.

The biphasic consolidation model was used to describe the deformation behavior of the tissue and has previously reported [11,18]. The inverse model is solved intraoperatively by an optimized least squared minimization between the model predicted displacements and displacements measured through homologous point selection in sparse intraoperative data [3]. The process of mesh construction and atlas generation is automated, but in [3], the segmentation steps were performed manually. The typical MRI image volume acquired had 180 slices in that study and the manual segmentation process was tedious and could take a few hours. In the following sections an automated segmentation process will be described and a comparison between the results of automatic and manual segmentation will be presented.

2.1 Data

The data consists of five image sets acquired pre-operatively for patients undergoing brain tumor removal surgery shown in Table 1. The scans were acquired using 1.5-T clinical scanner. The voxel size for

all patients was $1\text{ mm} \times 1\text{ mm} \times 1.2\text{ mm}$ and each scan consisted of 180 to 190 slices.

2.2 Automated Segmentation

The automated segmentation algorithm is based on the atlas-based segmentation approach described in [19]. The segmentation was performed using a series of three steps during which the patient images acquired above are registered to a template T1 image of size $256 \times 256 \times 256$ and $1\text{ mm} \times 1\text{ mm} \times 1\text{ mm}$ voxel size, for which an expertly segmented binary mask was available. The steps of the segmentation are described in Figure 2.

#	Location	Age, gender	Lesion size (cm)	Average measured shift (mm)	# selected points
1	L,F	22F	5.2 x 6.2 x 6.0	23.6	16
2	L,F	52M	4.9 x 5.6 x 5.0	15.1	22
3	L,P	58M	3.7 x 3.5 x 4.1	8.5	24
4	L,T	77M	3.4 x 3.6 x 2.0	9.2	18
5	L,T	75F	5.0 x 5.0 x 5.0	13.0	22

Table 1: Patient information about cases used in the study

The first step consisted of a rigid registration (T1) between the patient image and the template atlas image based on the mutual information metric [20]. The second step consisted of a non-rigid registration (T2) between the patient image and the transformed template image from first step using the adaptive basis algorithm driven with the mutual information metric [21]. The transformations obtained from the registrations (T1 and T2) are applied to the template mask to obtain a segmentation mask for the patient image. A set of template dural membrane structures were also created for the template image using the semi-automated method described in [3]. The registration transformations (T1 and T2) are then applied automatically to the dural septa structures – the falx cerebri and the tentorium cerebelli. The remainder of the tetrahedral mesh construction proceeds with the automated algorithm using [22, 23] as described in [3]. In addition to the automated segmentation described above, manually created expert segmentations were also performed for the structures. The closest point distances between the dural septa created by automated segmentation were compared to the manually segmented septa. The falx and the left and right tentorium were examined separately. In addition the falx was divided into three equally spaced regions – anterior, middle, and posterior region – and the closest point distances of these three regions were separately analyzed. Lastly, the difference between brain shift compensation results using the domains generated from these two different methods was compared.

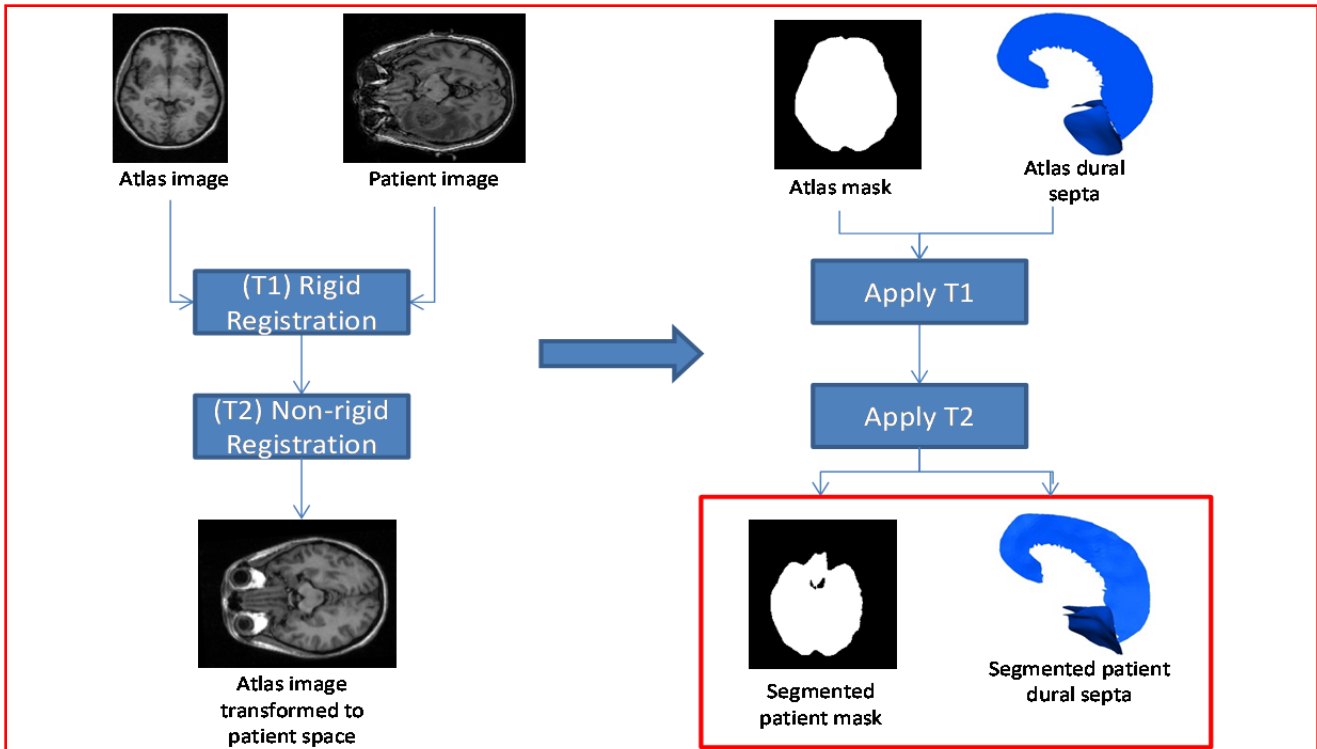


Figure 2: The schematic for segmentation of cerebral tissue and dural septa. A rigid transformation between an atlas image and patient image (T1) is computed. The transformation, T1 is applied to the atlas image and a non-rigid transformation (T2) is computed between the rigidly transformed atlas image and the patient image. The computed transformations (T1 and T2) are applied to structures derived from the atlas image (binary mask and dural septa templates) to obtain the segmentation of patient cerebral tissue and dural septa.

2.3 Sensitivity Analysis

The last step in the pre-operative pipeline in Figure 1 for atlas building involves constructing the boundary conditions based on the surgical plan and solving the model in a forward manner for each of those conditions, as described in greater detail in [12]. This process, though automated, may be the most time consuming computational step depending on the number of conditions for which the model is solved. For instance, in the work in [3], two different forces were modeled: gravitational force and force resulting from pressure gradients caused by hyperosmolar drugs like mannitol. For gravity, 60 head orientations were solved using 3 CSF drainage levels, each model solved with and without tumor resection – resulting in 360 solutions. Mannitol conditions were solved similarly with an atlas consisting of 360 solutions, resulting in a combined atlas of 720 solutions. The time for a single forward model solve varies depending on the uniformity of element size, the number of elements in the mesh, and hardware utilized. Our software has been built for parallel computations using the open-source software resources PETSc [24] and MPI [25] and all the

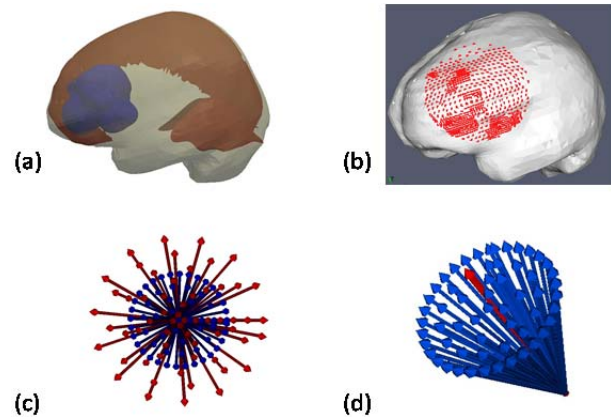


Figure 3: (a) Mesh used for the simulation experiments with the dural septa (brown) and the tumor (blue) overlaid, (b) The displacement solutions of the forward runs at the craniotomy nodes (red) used to simulate sparse data, (c) Spatial extent experiment. Blue shows the head orientations in that atlas. Red arrows show the head orientation of the ground truth solutions. (d) Spatial resolution experiment. Blue shows the head orientations in the atlas. Each orientation was eliminated from the atlas and used as the ground truth solution sequentially.

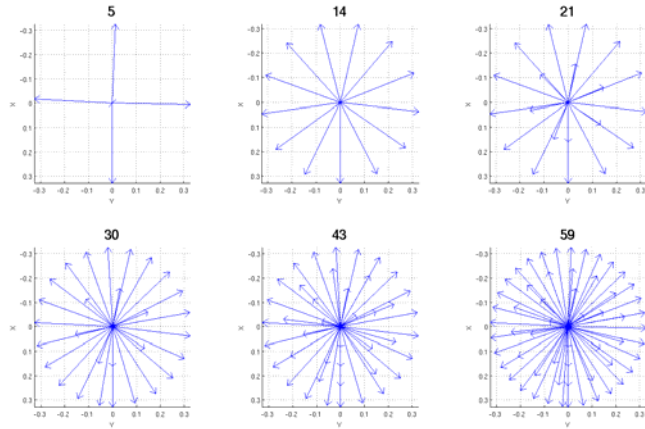


Figure 4: The number listed on top is the number of head orientations in each atlas. The different sized atlases were used to evaluate the effect of spatial resolution on the inverse model.

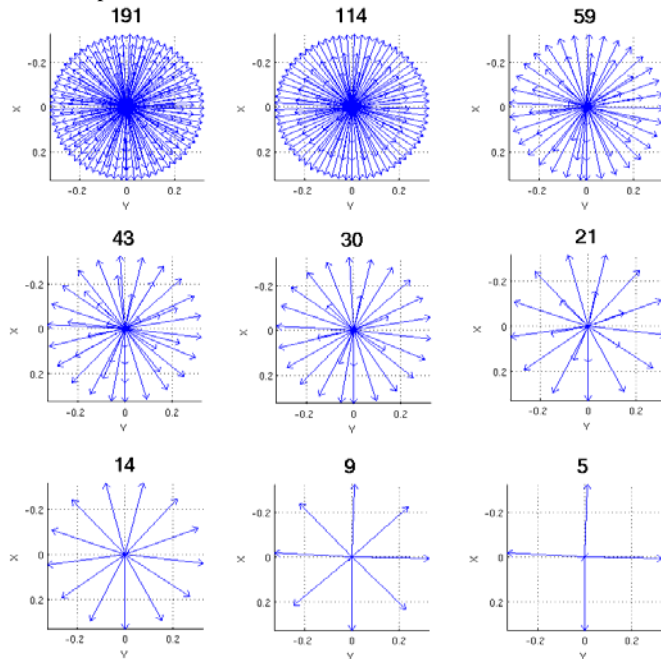


Figure 5: The number listed on top is the number of head orientations in each atlas. The different sized atlases were used to evaluate the effect of spatial resolution on the inverse model for the clinical data listed in Table 1.

orientations was systematically eliminated from the atlas and used as ground truth. This was repeated for six different atlases with different atlas solution sets of varying sparsity as shown in Figure 4 with the six atlases designating the number of contained solutions as 5, 14, 21, 30, 43, and 59, respectively. The correction results for every solution in the atlas was evaluated by running the inverse model and looking at the shift correction. In addition, the ‘ground truth’ selection was never contained explicitly within an atlas being used for correction.

Clinical data

The sensitivity of shift correction to number of head orientations, CSF drainage levels, and mannitol related capillary permeability values was also evaluated using the pre-operative MRI and intraoperative laser range scanner data collected

computations in [3] were performed with a parallel cluster of 12 quad-core 2400 MHz Dual-Core AMD Opteron(tm) Processors. The computations were distributed across four of these nodes and building time for an atlas with 720 solutions ranged from 10 to 18 hours. The following sub-sections will describe sensitivity studies using simulations and clinical data in Table 1 to evaluate the effect of atlas size on accuracy of the inverse model.

Simulation Experiments

The goal of the simulation studies was to evaluate the size and composition of the deformation atlas. Since the largest contribution to the atlas size came from the number of head orientations, this will be the main parameter studied in the simulation experiments.

For the simulation experiments, an FEM mesh from one of the clinical cases listed in Table 1 was used (Figure 3 (a)). Forward model runs with varying head orientations and other forcing conditions are used as ground truth. Sparse data was simulated by selecting the displacement solutions for the nodes in the craniotomy region, close to the tumor (Figure 3 (b)). In the first experiment, the effect of spatial extent was studied. In Figure 3 (c), the blue arrows (corresponds to the direction of the gravity vector) show the head orientation of each solution in the atlas, the extent of the cone is 20° . The red arrows show the head orientations corresponding to the ground truth (i.e. ground truth is the simulated results we would like to reconstruct from the atlas of solutions), consist of concentric cones ranging from 2.5° to 32.5° to the center, in the increments of 5° . The ground truth head orientations that are less than 20° from the center of cone are contained in the computed atlas. For solutions where the ground truth orientation was greater than 20° , the estimate of head orientation would be mispredicted and would lie outside the cone. In the second simulation experiment, the effect of spatial resolution was tested to study the effect of the size of the atlas on shift error (Figure 3(d)). Each of the head

for the five clinical cases listed in Table 1. To evaluate the effect of head orientations on clinical data, the different head orientations shown in Figure 5 were used to build the atlas. The atlas was also built using different fluid levels for gravity and different capillary permeability values for mannitol. The inverse model was tested with different numbers of fluid levels and capillary permeability values. Three fluid levels/capillary permeability was the maximum resolution used.

3. RESULTS

3.1 Automated Segmentation

Five cases in Table 1 were segmented using the automated algorithm as well as the manually. The results for automated segmentation of brain were assessed qualitatively as well as quantitatively. The occurrence of error for the segmentation of cerebrum was based on the visual evaluation of the quality of overlay between the segmentation mask and the cerebral tissue in the patient MRI. Slices that contained a visually significant misoverlap between the mask and the image were designated to contain error. The specific slices containing the segmentation errors were manually edited and the results were used for mesh construction and building the atlas. The following figure shows selected slices from a completely manual segmentation, automated segmentation and after editing the results of the automated segmentation for two cases.

The regions containing error, determined by qualitative evaluation of the overlay between the mask and the image, are designated with red arrows in Figure 6 (b) and (e) for two cases. Table 2 lists the total number of slices in each dataset and the number of slices for each case that contained segmentation error. Among the five datasets, for the automated segmentation of the cerebrum tissue, four of the cases had several slices containing some misclassified tissue and patient #3 was the only case that contained no segmentation error.

The results of the automated segmentation of the falx and tentorium were evaluated quantitatively as well as qualitatively. Through visual assessment of the dural septa, the automated segmentation algorithm provided acceptable results for modeling purpose. The segmentation results for the dural septa are shown in Figure 7. Figures 7 (a) – (e) show the surface of the finite element mesh and the dural septa – the falx and tentorium, created using the automated segmentation algorithm. The dural septa are color coded with the closest point distance between the septa segmented using the automated algorithm and the manual method. Figure 8 shows the average distance between the automatically and manually segmented dural septa. The distances for the falx, right, and left tentorium are presented separately. In addition, the falx is further subdivided into three equally spaced regions— anterior, middle and posterior. The overall average distance between the automatically and manually segmented dural septa is 3.7 ± 1.8 mm. The largest difference in terms of distances is in the anterior region of the falx. This is especially pronounced in patient #2, and to some extent in patient #1 and patient #4. The automatically (blue) and manually (red) segmented falx for patient #2 are shown in Figure 7 (f). The overlay of the falx and the tentorium on the MRI images are also shown for the same patient in Figure 7 (g) and Figure 7

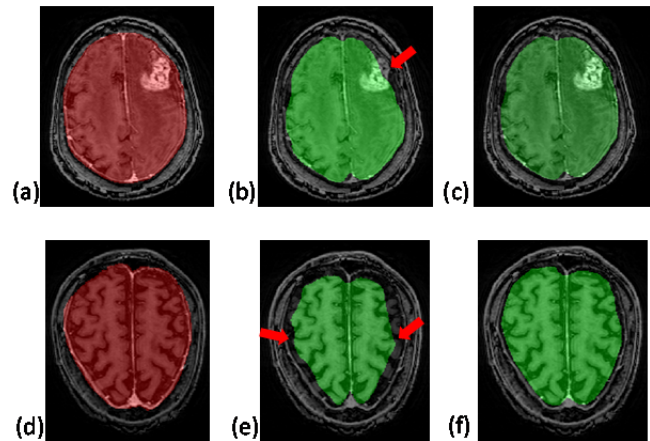


Figure 6: The top rows shows the segmentation results for patient #2 and the bottom row shows the segmentation results for patient #4. (a) and (d) show the results of manual segmentation. (b) and (e) show the results of automated segmentation with red arrows indicating the regions of misclassification of brain tissue. (c) and (f) show the slices in (b) and (e) after manually editing to correct the misclassified regions.

Case #	Total slices	# slices with segmentation errors
1	180	41
2	190	47
3	180	0
4	180	31
5	180	13

Table 2: Image size for each dataset and the number of slices in each dataset that got misclassified using the automated segmentation method.

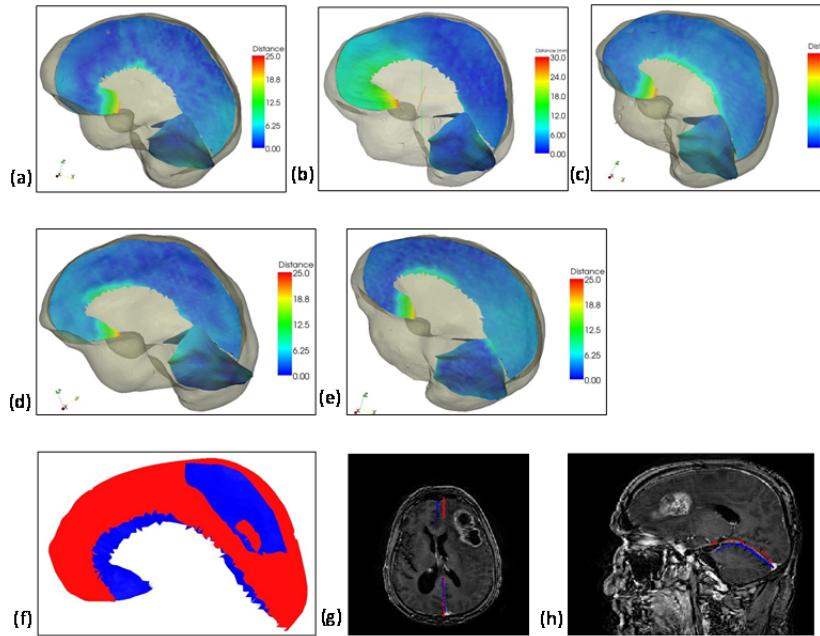


Figure 7: Shows the mesh along with the falx and tentorium segmented using the automated segmentation method. The falx and tentorium are color coded with the closest point distance between the automated and manually segmented dural septa (a) – (e) for patient 1 – 5 respectively. (f) shows the dural septa created by automated segmentation (blue) and manual segmentation (red), (g) shows the automated (blue) and manually segmented (red) falx overlaid on the MRI image and (h) shows the automated (blue) and manually segmented (red) tentorium overlaid on the MRI image for patient #2.

automated segmentation method is $73 \pm 13\%$. The mean correction was slightly lower for the automated segmentation method however a paired student t-test indicates that there is no statistical difference ($p > 0.05$) for the shift correction results using the two methods.

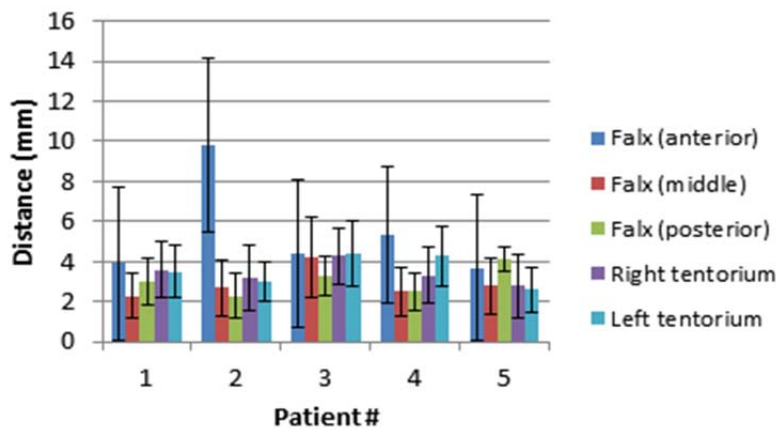


Figure 8: Shows the average closest point distances between the automatically and manually segmented dural septa for the five patient cases. The distances for anterior, middle, and posterior part of the falx, and right and left tentorium are presented separately.

error where the ground truth results were produced by simulating resection. In both the cases, the error is minimal when the actual head orientation is contained within the cone of head orientations used to construct the deformation atlas. The

(h) respectively. The blue lines are the results of the automated segmentation and the red contour is the results of manual segmentation. The overlay images also show least overlap between the two segmentation methods in the anterior region of the falx. The automated segmentation method actually performs better by visual evaluation of the overlay between the hyperintense region and falx contour. The tumor pushes the falx away from the centerline through mass effect and the manual segmentation of the falx was performed by drawing on the contour of the falx in the central sagittal plane and hence does not capture the deviation from the plane well, which is captured by the automated method. Figure 9 shows the percent shift correction after running the inverse model using the manual segmentation method and the automated segmentation method.

The average shift correction for the five cases using the manual segmentation method is $76 \pm 13\%$ and

3.2 Sensitivity Analysis

Simulation Experiments

The shift correction error for the simulation experiment for studying spatial extent, where the ground truth varied from 2.5° from center of the predicted cone of head orientations and up to 32.5° angle from the center is shown in Figure 10. The results for error between the location of model-predicted and ground truth points was averaged for each head orientation that was at the same angle from the center of the cone.

Figure 10(a) shows the results using the ground truth solutions without resection and Figure 10 (b) shows the error where the ground truth results were produced by simulating resection. In both the cases, the error is minimal when the actual head orientation is contained within the cone of head orientations used to construct the deformation atlas. The

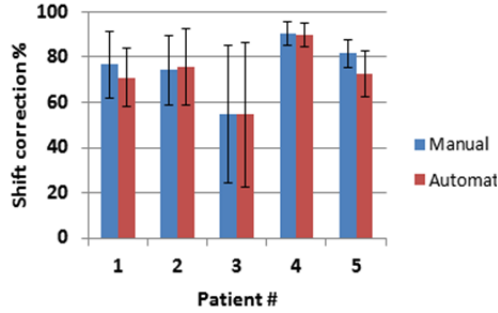


Figure 9. The percent shift correction between the measurements and the model predicted deformation for the five cases listed in Table 1 using the manual and automated segmentation methods.

error increases as the actual head orientation of the ground truth lies outside the sampling space of the head orientation angle. It is also a noteworthy point that the overall magnitude of error is larger for the case where ground truth simulates tissue resection.

The mean error and the standard deviation for each of the different sized atlases (Figure 4) are shown in Figure 11. Figure 11 shows that though the error is modestly larger for the atlas with the coarser resolution and then quickly becomes asymptotic for both surface and subsurface nodes.

Clinical data

Figure 12 shows the error between model prediction and measurements for the five clinical cases listed in Table 1 using

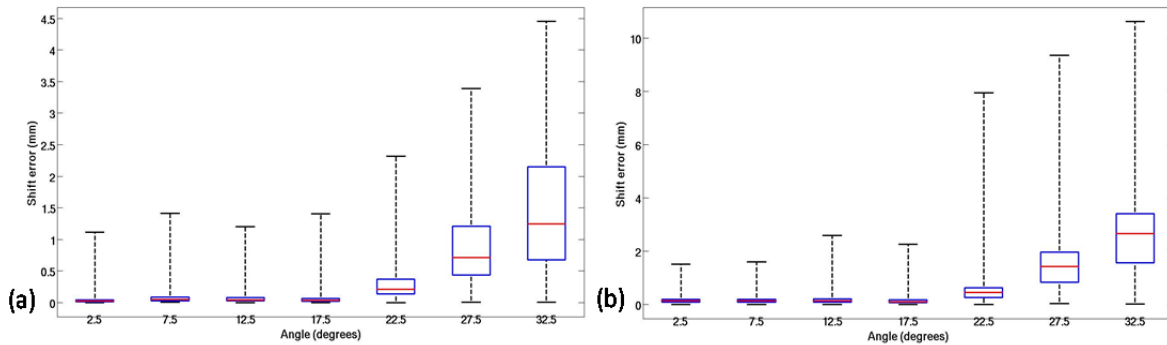


Figure 10: Box and whisker plot for error between model prediction and measurements for the simulation experiment. The x-axis represents the angle from the center of cone of atlas of head orientations and head orientation used to generate the ground truth. The red line represents the median, the box represents the twenty fifth and seventy fifth percentiles and the whiskers represent the extent of data. (a) shows the errors for ground truth without resection and (b) shows the ground truth with resection.

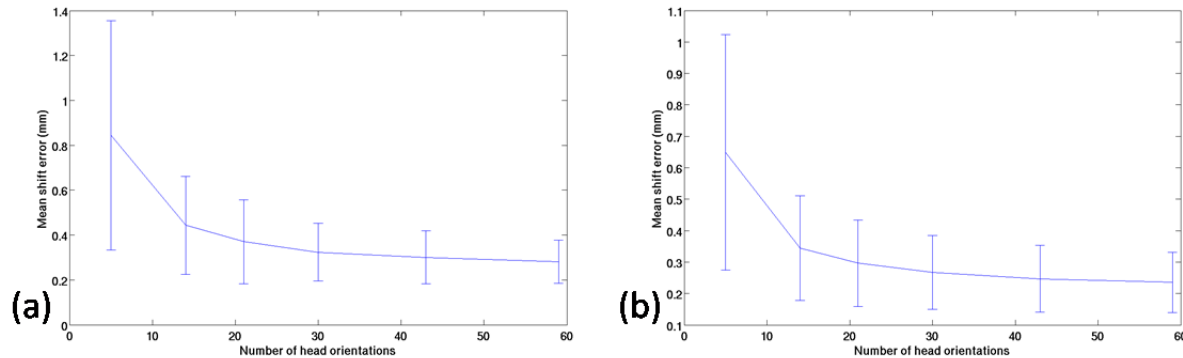


Figure 11: The mean and standard deviation of shift error for atlas of different resolution for (a) surface points and (b) subsurface points.

atlases built with different number of head orientations (Figure 5). The clinical data in Figure 12 follows a similar trend as the simulation experiment results in Figure 11, being larger at the coarser resolution and becoming asymptotic at larger resolutions with an accompanying decrease in variance. Although the above figure shows a maximum atlas size of 59 head orientations, larger sizes (shown in Figure 5) were also tested and showed no change. Testing for the effect of altering the number of fluid levels and capillary permeability values showed no change in shift correction results for the clinical cases.

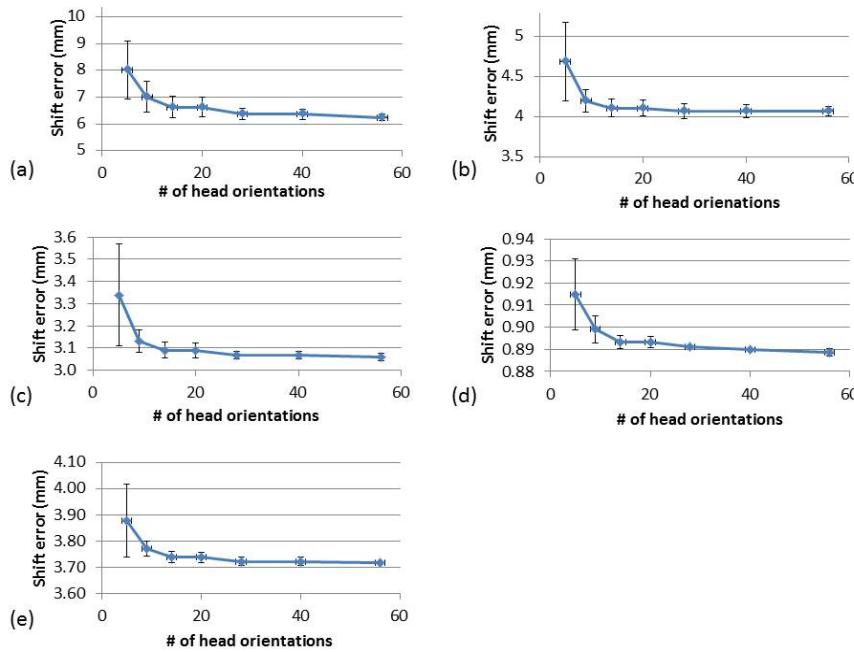


Figure 12: Shift error in mm, plotted for the five different cases, (a–e) correspond to patient #1–5. The error was calculated using atlas constructed with different number of head orientations, as shown in Figure 4.

4. DISCUSSION

The non-rigid deformation of the brain tissue caused by gravitational forces, hyperosmotic drugs, resection and retraction forces can result in a significant error, affecting the fidelity of the image guidance system in neurosurgery. The past literature has described combining the use of sparse intraoperative devices with computational models. Our group proposed the atlas-based paradigm to overcome the uncertainty of determination of various parameters in the intraoperative environment and we validated this method with retrospective studies using postoperative and intraoperative data [3, 17]. As we move towards the implementation of this method in real-time in the OR, the computational time and efficiency become important factors. This

work examines the pre-operative pipeline that consists of constructing the patient specific finite element mesh and building the deformation atlas. More specifically, an automatic segmentation method for the cerebrum and the dural septa was evaluated and the results of sensitivity analysis to determine the constitution of the deformation atlas were presented.

The automatic segmentation method for the cerebral tissue in the MR images was tested on five patient images and four of these datasets contained some error determined by visual examination. Since the segmentation method was based on the intensity based registration and the template image was a normal brain, anomalies in the images resulted in segmentation error. The results for hyperintensity on the surface due to large tumors and cerebral atrophy caused localized segmentation errors as demonstrated in Figure 6. Patient 2 had a tumor near the surface in the frontal lobe and the automated segmentation algorithm is confounded in the vicinity of that region. Patient #4 was a 77 year old male and the MRI of the brain shows age related cerebral atrophy. Consequently the automated algorithm did not perform well near the contours. Patient #3 was the only case where no substantial segmentation error was observed because in this case the bulk of tumor was beneath the surface. The other four cases, a handful of slices (ranging from 13 to 47 for the five cases) required manual editing as opposed to a completely manual segmentation method. For a completely manual segmentation of the image with 180 slices, takes an average of 2 to 3 hours. The automatic segmentation algorithm took about 15 minutes on a 3.2GHz, Intel I7 processor. Depending on the slices needing manual editing, the total time for segmentation, including the automated algorithm and manual editing, takes 30 minutes to an hour.

The results for the automatic segmentation of the dural septa are dependent on the results from the previous segmentation of cerebrum – it uses the transformations obtained from the rigid and non-rigid registration between the template image and the dataset. The algorithm produced segmentation results for falx and tentorium that were satisfactory for modeling purposes for all five cases. As seen in Figure 8, the automated segmentation technique did not significantly change the shift correction. The results of falx segmentation are visually more accurate using the automatic segmentation method because the manual method in [3] assumed it to be a planar structure, which is invalid when the mass effect from the

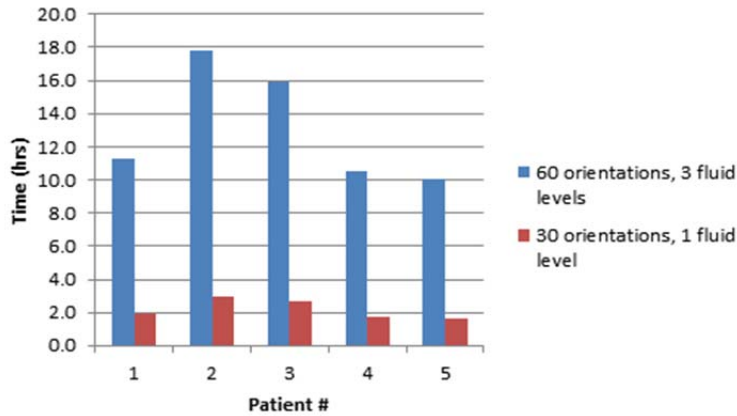


Figure 13: Computational time to build the pre-operative deformation atlas. The times are shown for 60 head orientations and 3 fluid levels as in [3]. This is compared to the computational time for a smaller atlas with 30 head orientations and 1 fluid level.

tumor pushes the structure away from the plane. The largest benefit of the automatic segmentation for both the cerebrum and the dural septa is the reduction in time. As discussed before, the complete manual segmentation of the cerebral tissue takes 2 - 3 hours. The semi-automatic segmentation of the dural septa takes an additional 15 - 30 minutes. Even with manually correcting the segmentation errors for a few slices, the computational time ranges from 30 minutes to an hour, giving a time savings of 1.5 to 3 hours.

The number of head orientations is the variable that contributes the maximum number of solutions to the size of the atlas. Using simulation experiments, spatial extent was found to be a more important factor in

the shift correction accuracy than the resolution. Considerably larger errors were found when the true orientation was outside the prediction sample space as shown in Figure 10. Sampling the space more finely does not significantly improve the shift correction as seen in both the simulation study (Figure 11) and the clinical data (Figure 12). At the minimal number of head orientations, the error is slightly higher, but the correction error is asymptotic at 20–30 solutions. Using different number of fluid levels and permeability values resulted in no change in shift correction results. This could be explained based on the constrained optimization method used to reconstruct the inverse model results. As shown in [3], the optimization method minimizes the least squared error between the measurements and predictions with the non-negativity constraint and the summation of all weighting coefficients being less than or equal to one. The fluid levels and capillary permeability values control the magnitude of shift, and if the magnitude of measurement is smaller than the predictions, then the weighting coefficients interpolate it with the appropriate scaling.

Figure 13 compares the computation time for building the atlas using 60 head orientations and three fluid levels/capillary permeability values as done in [3] and 30 head orientations and one fluid level/capillary permeability value. The average time with 60 orientations and three fluid levels/capillary permeability values is 13.1 ± 3.5 hours, whereas the average computational time for building the atlas with 30 head orientations with one fluid level/capillary permeability value is 2.2 ± 0.6 hours. The change in shift error by reconstructing the results from these two atlases is minimal but the savings in time cost is significant.

5. CONCLUSION

In the study described above, a limited number of cases were used. While the automatic segmentation method only resulted in localized errors, if the patient image is sufficiently different from the template image, it is possible for the image intensity based segmentation method to fail, which would necessitate manual segmentation of both the cerebrum and the dural septa. The automatic segmentation reduces the time of computation and cumbersome manual editing, although it does not obviate a review of the segmentation. The results of the sensitivity analysis show that the pre-operative computational time can be further reduced several-fold by decreasing the sampling resolution of the atlas without significantly degrading the shift correction. The time window from the time the pre-operative MR images are acquired to the beginning of the neurosurgery can vary from a few hours to several days. In the atlas-based inverse model paradigm, the bulk of the computational cost is shifted pre-operatively, and therefore it is important that those computations be completed within that time window. The findings in this study will have important implications in ensuring the completion of pre-operative computations within the time constraints for the implementation of the atlas-based method in real time.

Acknowledgements: This work has been supported by the National Institutes of Health (NIH)—National Institute of

Neurological Disorders and Stroke under Grant R01 NS049251. The authors would like to thank the resident surgeons, the operating room staff and the radiology department at Vanderbilt University for their help in data collection. Most of the visualization algorithms were developed using Visualization Toolkit (<http://www.vtk.org>).

6. REFERENCES

- [1] D. W. Roberts, A. Hartov, F. E. Kennedy, M. I. Miga, and K. D. Paulsen, "Intraoperative brain shift and deformation: A quantitative analysis of cortical displacement in 28 cases," *Neurosurgery*, vol. 43, no. 4, pp. 749-758, Oct, 1998.
- [2] C. Nimsy, O. Ganslandt, S. Cerny, P. Hastreiter, G. Greiner, and R. Fahlbusch, "Quantification of, visualization of, and compensation for brain shift using intraoperative magnetic resonance imaging," *Neurosurgery*, vol. 47, no. 5, pp. 1070-1079, Nov, 2000.
- [3] I. Chen, A. M. Coffey, S. Ding, P. Dumpuri, B. M. Dawant, R. C. Thompson, and M. I. Miga, "Intraoperative brain shift compensation: accounting for dural septa," *IEEE Trans Biomed Eng*, vol. 58, no. 3, pp. 499-508, Mar, 2011.
- [4] W. E. Butler, C. M. Piaggio, C. Constantinou, L. Nikalson, R. G. Gonzales, G. R. Cosgrove, and N. T. Zervas, "A mobile computed tomographic scanner with intraoperative and intensive care unit applications.," *Neurosurgery*, vol. 88, no. 4, pp. 1304-1310, 1998.
- [5] M. M. J. Letteboer, P. W. A. Willems, M. A. Viergever, and W. J. Niessen, "Brain shift estimation in image-guided neurosurgery using 3-D ultrasound," *IEEE Transactions on Biomedical Engineering*, vol. 52, no. 2, pp. 268-276, Feb, 2005.
- [6] D. Gobbi, R. Comeau, and T. Peters, "Ultrasound Probe Tracking for Real-Time Ultrasound/MRI Overlay and Visualization of Brain Shift," *Medical Image Computing and Computer Assisted Intervention: Lecture Notes in Computer Science*, vol. 1679, pp. 920-927, 1999.
- [7] D. Gobbi, R. Comeau, and T. Peters, "Ultrasound/MRI Overlay with Image Warping for Neurosurgery," *Medical Image Computing and Computer Assisted Intervention: Lecture Notes in Computer Science*, vol. 1935, pp. 29-53, 2000.
- [8] M. Ferrant, A. Nabavi, B. t. Macq, F. A. Jolesz, R. Kikinis, and S. K. Warfield, "Registration of 3-D Intraoperative MR Images of the Brain Using a Finite-Element Biomechanical Model," *IEEE Transactions on Medical Imaging*, vol. 20, no. 12, pp. 1384, 2001.
- [9] A. Wittek, K. Miller, R. Kikinis, and S. K. Warfield, "Patient-specific model of brain deformation: Application to medical image registration," *Journal Of Biomechanics*, vol. 40, no. 4, pp. 919-929, 2007.
- [10] O. Clatz, H. Delingette, I-F. Talos, A. J. Golby, R. Kikinis, F. Jolesz, N. Ayache, and S. Warfield, "Robust non-rigid registration to capture brain shift from intraoperative MRI," *IEEE Transactions on Medical Imaging*, vol. 24, no. 11, pp. 1417-1427, 2006.
- [11] M. I. Miga, K. D. Paulsen, J. M. Lemery, S. D. Eisner, A. Hartov, F. E. Kennedy, and D. W. Roberts, "Model-updated image guidance: Initial clinical experiences with gravity-induced brain deformation," *IEEE Transactions on Medical Imaging*, vol. 18, no. 10, pp. 866-874, 1999.
- [12] P. Dumpuri, R. C. Thompson, B. M. Dawant, A. Cao, and M. I. Miga, "An atlas-based method to compensate for brain shift: Preliminary results," *Medical Image Analysis*, vol. 11, no. 2, pp. 128-145, 2006.
- [13] N. Hata, T. Dohi, S. K. Warfield, W. M. Wells III, R. Kikinis, and F. A. Jolesz, "Multimodality Deformable Registration of Pre- and Intraoperative Images for MRI-guided Brain Surgery," *Proceedings of the First International Conference on Medical Image Computing and Computer-Assisted Intervention*, vol. 1496, no. 1998, pp. 1067-1074, 1998.
- [14] H. Sun, D. W. Roberts, H. and Farid, Z. Wu, A. Hartov, and K. D. Paulsen, "Cortical Surface Tracking Using a Stereoscopic Operating Microscope," *Neurosurgery*, vol. 56, no. 1, pp. 86-97, 2005.
- [15] M. A. Audette, K. Siddiqi, F. P. Ferrie, and T. M. Peters, "An integrated range-sensing, segmentation and registration framework for the characterization of intra-surgical brain deformations in image-guided surgery," *Computer Vision and Image Understanding*, vol. 89, no. 2-3, pp. 226-251, Feb-Mar, 2003.
- [16] T. K. Sinha, B. M. Dawant, V. Duay, D. M. Cash, R. J. Weil, and M. I. Miga, "A method to track cortical surface deformations using a laser range scanner," *IEEE Transactions on Medical Imaging*, vol. 24, no. 6, pp. 767-781, 2005.

- [17] P. Dumpuri, R. C. Thompson, A. Cao, S. Ding, I. Garg, B. M. Dawant, and M. I. Miga, "A fast efficient method to compensate for brain shift for tumor resection therapies measured between preoperative and postoperative tomograms.," IEEE Transactions on Biomedical Engineering, vol. 57, no. 6, pp. 1285-1296, 2010.
- [18] M. A. Biot, "General Theory of Three-Dimensional Consolidation," Journal of Applied Physics, vol. 12, no. 2, pp. 155-164, 1941.
- [19] P.-F. D'Haese, V. Duay, T. E. Merchant, B. Macq, and B. M. Dawant, "Atlas-Based Segmentation of the Brain for 3-Dimensional Treatment Planning in Children with Infratentorial Ependymoma," Proc. MICCAI, pp. 627-634, 2003.
- [20] F. Maes, A. Collignon, D. Vandermeulen, G. Marchal, and P. Suetens, "Multimodality image registration by maximization of mutual information," Medical Imaging, IEEE Transactions on, vol. 16, no. 2, pp. 187-198, 1997.
- [21] G. K. Rohde, A. Aldroubi, and B. M. Dawant, "The adaptive bases algorithm for intensity-based nonrigid image registration," Medical Imaging, IEEE Transactions on, vol. 22, no. 11, pp. 1470-1479, 2003.
- [22] J. M. Sullivan, G. Charron, and K. D. Paulsen, "A three-dimensional mesh generator for arbitrary multiple material domains," Finite Elements in Analysis and Design, vol. 25, no. 3-4, pp. 219-241, 1997.
- [23] M. I. Miga, K. D. Paulsen, F. E. Kennedy, P. J. Hoopes, A. Hartov, and D. W. Roberts, "In Vivo Analysis of Heterogeneous Brain Deformation Computations for Model-Updated Image Guidance," Comput Methods Biomech Biomed Engin, vol. 3, no. 2, pp. 129-146, 2000.
- [24] S. Balay, W. D. Gropp, L. C. McInnes, and B. F. Smith, Modern Software Tools in Scientific Computing, pp. 163-202, Ann Arbor, MI: Birkhauser Press, 1997.
- [25] H. El-Rewini, and M. Abd-El-Barr, Message Passing Interface (MPI), in Advanced Computer Architecture and Parallel Processing, Hoboken, NJ: John Wiley & Sons, Inc., 2005.